Latching ultra-low power MEMS shock sensors for acceleration monitoring

Luke J. Currano [a,d,*], Scott Bauman [b], Wayne Churaman [c], Marty Peckerar [b], James Wienke [b], Seokjin Kim [b], Miao Yu [d], Balakumar Balachandran [d]

a U.S. Army Research Laboratory, 2800 Powder Mill Road, Adelphi, MD 21046, United States
b Electrical and Computer Engineering, University of Maryland, College Park, MD 20742, United States
c General Technical Services, 3100 Route 138 Building 3, Wall Township, NJ 07719, United States
d Department of Mechanical Engineering, University of Maryland, College Park, MD 20742, United States

ABSTRACT

A microelectromechanical shock sensor, which uses a latching mechanism to record a shock event above a specified threshold level, is discussed in this article. The fabrication process for the shock sensor, which includes wafer-level vacuum packaging, is detailed along with the design features. These features include a reset actuator for reuse of the sensor, a no-power operation scheme when the reset actuator is not activated, and a control circuit to minimize power used to unlatch the sensor. In order to describe the shock-sensor dynamics and interaction with the latch mechanism, a preliminary non-linear model has been developed. Experimental results are presented and compared with model predictions.

Published by Elsevier B.V.

1. Introduction

Health monitoring of critical systems is gaining increasing attention due to the availability of inexpensive, miniature, low-power sensors [1,2]. Two fundamental approaches to carry out this monitoring are as follows: (i) monitoring of the system performance and (ii) monitoring of the environment in which the system is located. Each of these approaches has its own benefits. On one hand, implementation of environmental monitoring is typically simple, while on the other hand, performance monitoring is more directly linked to system health. Historically, specification sheets list allowable environmental conditions, and environmental monitoring can be used to determine if the allowed specifications are exceeded. Due to the ease of implementation and the available specifications, environmental monitoring is currently the more commonly used approach.

The present work is motivated by a need to create a rudimentary acceleration sensor that uses minimal power. Power requirements for environmental monitoring systems are often severely limited, especially for long life time systems. Low-power sensors are critical to enabling embedded health monitoring where power is not readily available. For example, a piece of ammunition may be stored for

10 years or more on a pallet in a warehouse before being required to perform its function with near-perfect reliability. Many different types of sensors can be used to measure different environmental factors, but the most common quantities of interest are temperature, humidity, and vibration levels in the form of acceleration. In general, for slowly varying quantities (say temperature and humidity), the sensors are easy to implement in a low-power package. The sensors can be powered down most of the time and powered up in intervals to record measurements without missing important events. However, this architecture is not viable for vibration (say, acceleration) measurements, which are characterized by quick changes.

The shock sensor described in this article provides a solution to ultra-low power acceleration monitoring by incorporating a mechanical acceleration switch. When the system exceeds a designed acceleration threshold level, the switch is triggered and an electrical circuit is closed. Hence, this sensor can then be used to provide a wake-up signal for a conventional accelerometer to gather more detailed information about a drop event, for instance, including absolute acceleration spectral content and magnitude. Alternatively, the shock sensor itself can be used to carry out a simple pass–fail test to assess the health of the system, by storing the shock event indefinitely until queried to determine if the system had been dropped or improperly handled. In this configuration, multiple sensors designed for different threshold levels or response times can be used to provide basic information about the severity of a shock event.

* Corresponding author at: U.S. Army Research Laboratory, 2800 Powder Mill Road, Adelphi, MD 21046, United States. Tel.: +1 301 394 0566.
E-mail address: lcurrano@arl.army.mil (L.J. Currano).

A handful of similar devices have been reported in the literature [3–5]. By and large, the earlier efforts have focused on sensor fabrication. Apart from the fabrication process, the uniqueness of this work is derived from the following: (i) development of a mechanical model that takes into consideration the non-linear interaction between the shock sensor and latching mechanism including friction, (ii) experiments carried out with the shock sensors and comparisons of shock table test data with model predictions, and (iii) implementation of an ultra-low power feedback control system for sensor reset and re-actuation. From a design standpoint, the modeling and experimental contributions should facilitate better analysis and prediction of sensor performance. In addition, the control circuit should enable a fail-safe reset operation with minimum power.

The rest of the article is organized as follows. In the next section, sensor design and fabrication are detailed. A model of the sensor is provided in Section 3, and a control circuit for unlatching and resetting the device is presented in Section 4. Next, the results are presented and discussed, along with concluding remarks.

2. Sensor design and fabrication

For purposes of illustration, the focus of this article is limited to two shock sensors. These sensors trigger at threshold root-mean-square acceleration levels of 37.5 g and 75 g, respectively. The overall sensor dimensions (including the wire-bond pads and reset actuators) are approximately 4 mm × 6.5 mm for the 37.5 g design and 4 mm × 5.7 mm for the 75 g design. The other sensors, which have been fabricated by using the same process and design, are in the acceleration range of 10–150 g.

2.1. Design

The sensor consists of a series of springs attached to the substrate at one end and the mass at the other, as shown in Fig. 1. The pictured device uses a two-fold symmetric design with four springs to reduce the sensitivity to off-axis and rotational accelerations compared with single and dual-spring configurations. When the system undergoes an acceleration along the *y*-axis, the motion of the mass forces two springs into compression and the other two springs into extension. The sensor incorporates latches anchored to the substrate, which engage the mating pieces attached to the mass after the sensor has traveled the designed setback distance
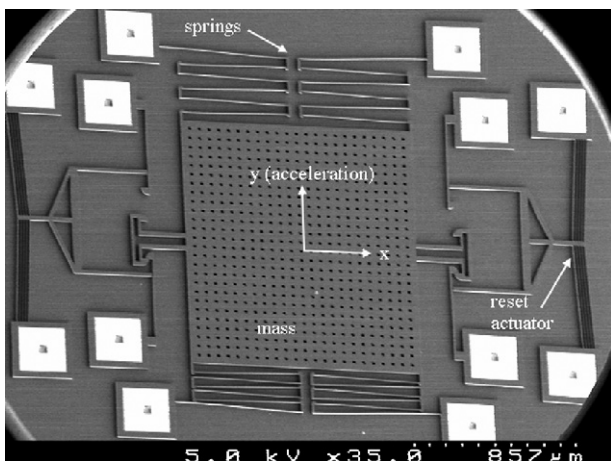

Fig. 1. Shock sensor (shown in latched position). The mass is in the center, the springs are at the top and bottom, and the reset actuators are at the far left and far right.
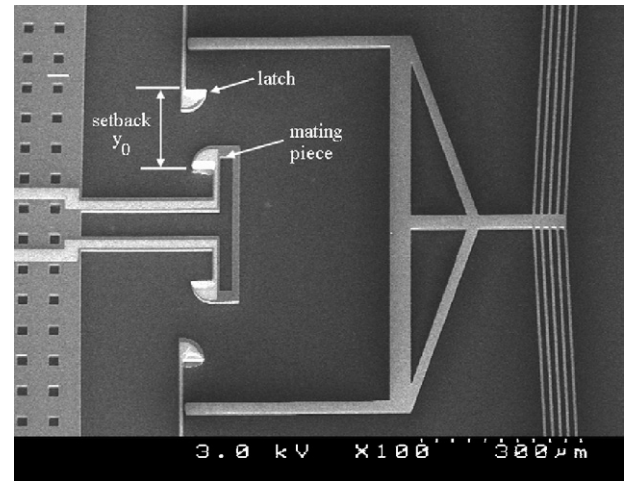

Fig. 2. Close-up of the latch and release mechanism.

(see Fig. 2). The latches are cantilevered so that they are stiff in the direction of travel of the mass and less stiff in the direction normal to the direction of travel. This allows them to move out of the way as the mass pushes past them. Four latches are used in this device with two of them meant for positive acceleration and the other two meant for negative acceleration along the same axis. Once the mass engages the latches in either the positive or the negative displacement direction, an electrical circuit is closed between the two latches. This serves as the shock-detection mechanism.

The sensor is reset following the detection and recording of the shock event by using thermal actuators that are shown on the far left and right sides of the image (Fig. 1). Here, V-beam style thermal actuators (also called bent-beam actuators) are used, since the authors' prior experience indicates that it is difficult to get sufficient force with U-beam style actuators (also called hot-beam/cold-beam actuators). The bent-beam actuators have been described in previous studies [6–8], and here, for clarity, a brief description of their operation is provided. The baseline actuator is a conductive beam divided into two segments that are rotated in-plane slightly by design to give the full beam a "V" shape. When current is driven through the beam, Joule-heating causes thermal expansion of each segment. Since the beam structures are fixed at the ends, the two segments push against each other and generate an in-plane motion in the direction they are pointed towards. Due to the shallow angle and slender beam profile required for thermal strain amplification of the V-beam structure, most of the generated force is not along the actuation direction. The force component that is not along the actuation direction axially compresses the V-beam structure. If this axial force component is large enough to cause buckling of the structure, the output force from the actuator can drop dramatically. However, multiple beam structures can be used in parallel to overcome this limitation.

In the present work, the required actuation force to reset the shock sensor necessitated the use of five parallel beam structures. For the chosen V-beam dimensions (5 μm width and 600 μm length), a minimum of five beams is required to reliably unlatch the device while avoiding buckling of the individual V-beams. The actuators here push against the latches to disengage them from the mass. It is worth noting that the reset actuators are not connected to the latches; there is a gap of 3 μm in between them and this gap can be seen in Fig. 2.

In principle, the design can be extended to sense shock levels lower than 37.5 g or shock levels higher than 75 g. The primary difficulty associated with low shock levels is stiction, since the mass

shown in Fig. 1 needs to be large and the springs need to be more compliant as the threshold level is decreased. In the authors' experience, latching shock sensors with threshold levels below 25 g are quite difficult to realize. The main concern in extending the design to higher threshold levels is wear and fracture of the silicon components resulting from the impact of the mass on the latches. The authors have not yet explored the upper limits on the threshold levels realizable with the present design.

2.2. Fabrication

The mass, spring, latches, and reset actuator of the sensor are made of low-resistivity silicon (1–$3\,m\Omega\,cm$) to lower the voltage required by the actuators and the resistance of the sensor in the latched-state. The sensor is fabricated on a silicon-on-insulator (SOI) wafer with a 20-μm thick device layer, a 2 μm buried oxide layer, and a 500-μm thick, 1–$10\,\Omega\,cm$ handle wafer. Chrome gold (Cr/Au) wire bonding pads are deposited first on the anchors of each of the springs, latches, and actuators. Gold–tin (AuSn 80/20) rings are then deposited around each of the anchors to provide for wafer-to-wafer bonding with a cap wafer later in the process. Next, the complete device profile, including springs, mass, latches, and actuators, is patterned and deep reactive ion etching (DRIE) is used to transfer the profile to the silicon device layer in a single step. The wafer is re-patterned with a thick negative photo-resist that allows patterning over features up to about 30 μm and sputtered CrAu or aluminum is deposited on the mating sidewalls of the latches to lower the contact resistance. The last patterning step on the device wafer is a backside DRIE of trenches about 375 μm deep and 100 μm wide in between the individual die to provide cleaving lines for die separation.

Attempts to release the device in a standard liquid HF/supercritical drying process were found to be unreliable. Many of the devices ended up stuck to the wafer due to the large mass and relatively compliant springs. Therefore, the authors switched to a vapor-phase HF release process, performed in a Primaxx MEMS-CET etcher that provided good results with no stiction or residue; this etcher is also less aggressive in attacking the Cr adhesion layer under the bond pads.

Vacuum packaging reduces the power required for the reset actuators dramatically, since the dominant loss mechanism is heat transfer through the air into the underlying substrate. This has been observed before for thermal actuators [6]. Vacuum probe station tests on the fabricated devices have shown that a sensor that resets at 15 V/108 mA in air at atmospheric pressure will reset at 7 V/50 mA at an air pressure of 140 mT. Further characterization is needed to determine the pressure levels up to which the benefit of the low surrounding pressure can be utilized.

The authors developed a AuSn wafer-level vacuum packaging process to lower the reset actuator current and voltage (see Fig. 3). The procedure for this process is as follows. First, a silicon dioxide layer 0.5 μm thick is deposited on a second double-side-polished silicon wafer (standard, not SOI). Subsequently, AuSn rings matching those on the device wafer are deposited on top of the oxide layer via e-beam evaporation. The oxide layer is removed in the area inside the ring with an RIE etch. On the opposite side of the cap wafer, cleaving lines and through holes are etched about 375 μm deep by using DRIE. The cleaving lines match those in the device wafer. This first part of the through holes is substantially wider than the bond pads to accommodate a wire bonding capillary. These holes are then finished from the front side of the cap wafer with another DRIE; this part of the hole is smaller than the diameter of the AuSn ring. The cap wafer is then aligned and bonded to the device wafer with a AuSn eutectic bond, at a temperature of 300 °C
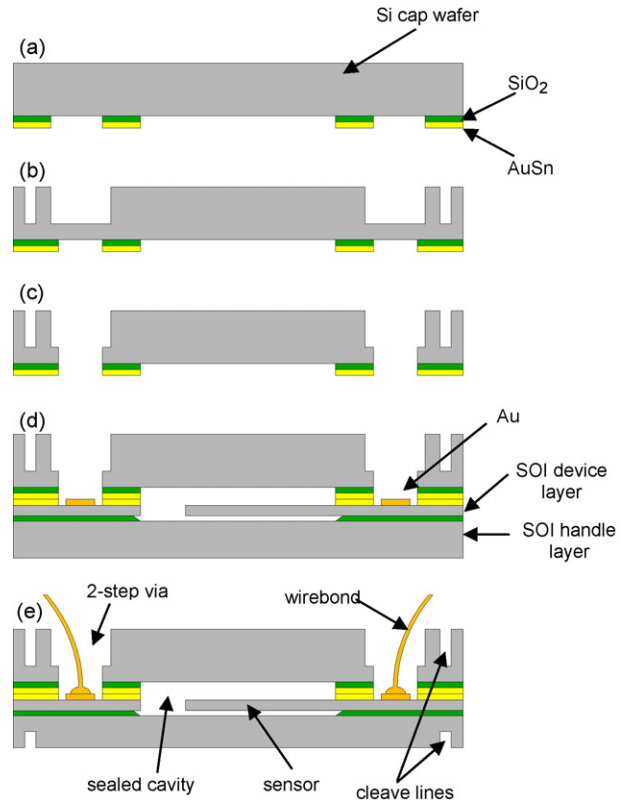

Fig. 3. Wafer-level packaging process: (a) deposition and patterning of oxide insulting ring and AuSn bond rings on cap wafer, (b) 375 μm backside etch in cap wafer for cleaving lines and wide part of through hole, (c) frontside etch of capwafer to finish narrow part of through hole, and (d) bond cap wafer to device wafer using AuSn eutectic bond.

in a 50T H_2N_2 atmosphere by using 1 PSI bond pressure. The result of this packaging process is that the device bond pads are exposed to the environment so that electrical contact can be made, while the sensor is contained in a sealed chamber (see Fig. 3). Electrical connection between the sensor and the bond pads is accomplished through the low-resistivity silicon device layer of the SOI wafer.
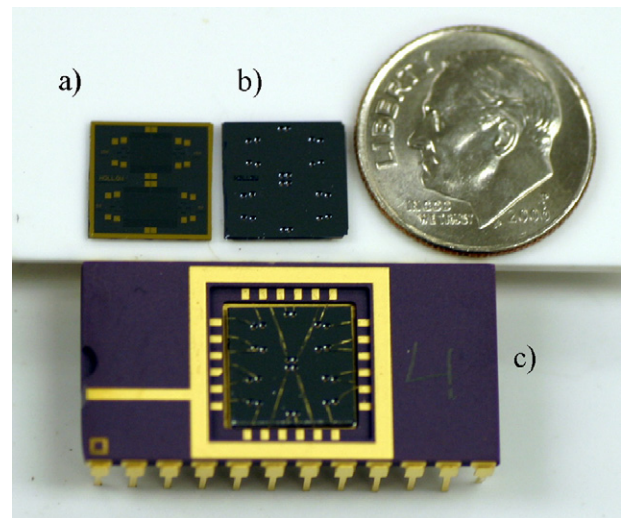

Fig. 4. Electronic package: (a) unpackaged die, (b) wafer-bonded die, and (c) wafer-bonded and wire-bonded shock sensor die. Each die has two sensors, one designed to trigger at 37.5 g acceleration and the other at 75 g acceleration.

The wafer is either cleaved apart or diced, and the individual sensors are placed in an electronic package and wire bonded (see Fig. 4). It is worth noting that each of the springs is wire bonded to a pin-out on the package for diagnostic use. The resistance between each of the springs can be checked to determine if the spring is intact or broken. The typical spring–spring resistance in the fabricated devices is about 5 kΩ.

One issue that the authors encountered with the bonding process was that the Cr/Au bond pads sometimes showed discoloration and bubbles after bonding (see Fig. 5). This is believed to be due to pinholes in the bond pads, which allow the underlying chromium to be attacked by the vapor HF. The bond pads appeared undamaged after the release process, but when the wafer is heated above 275 °C, a reaction apparently takes place between the gold and the silicon substrate causing the bubbles and discoloration. Attempts to wire bond to the damaged bond pads failed, since the wire bond would not stick to the pad. By increasing the thickness of the gold layer from 2000 Å to 4000 Å, it is found that the pinholes could be eliminated and the bond pads remained intact after bonding.

3. Preliminary model and simulation results

A model for the operation of the shock sensor is developed in this section. As a first step in the modeling, the system is assumed to be undamped, and static considerations are used to determine the contact force between the latch and the mating piece on the mass. The latch and the mating piece are modeled as smooth quarter-circle arcs. The contact between the latch and the mass is assumed to be steady after contact is made, with no bouncing. Gravity is assumed to be normal to the plane of the device motions. The following notations are used throughout this section.

m equivalent sensor mass
k equivalent sensor spring constant
k_1 equivalent latch force constant
F_y force exerted on mass by latch in y-direction
F_x force exerted on mass by latch in x-direction
$y_{m/c}$ distance traveled by mass with respect to chip
$\ddot{y}_c$ acceleration of chip
N normal force exerted by latch on mass
F_f friction force exerted by latch on mass
θ contact angle between mass and latch
y_0 initial distance mass must travel to pass latch
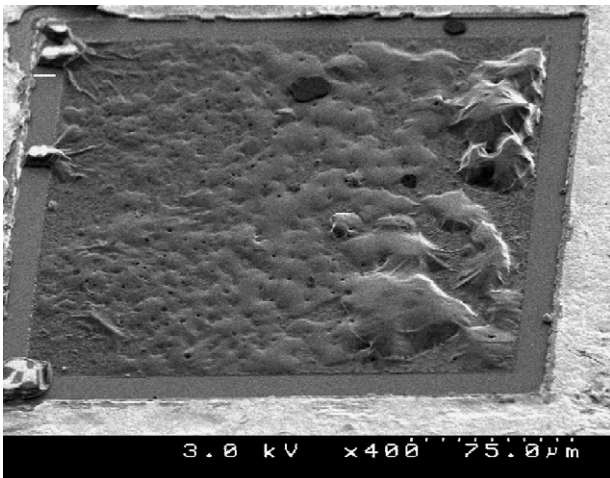r radius of curvature of latch

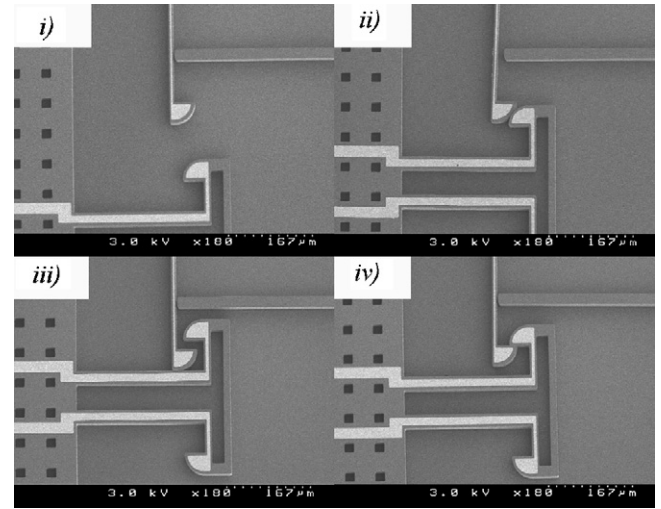**Fig. 5.** Damaged bond pad after wafer bonding.

Fig. 6. Different phases of mass-latch interaction of the shock sensor.

d_i initial offset of latch from mass in x-direction
μ static coefficient of friction

The operation of the shock sensor can be divided into four distinct phases (see Fig. 6): (i) a phase before the mass contacts the latch, (ii) a phase where the two are in contact and the mass is pushing past the latch, (iii) a phase where the mass has moved all the way beyond the latch, and (iv) a phase where the mass has settled back against the latch into its resting state. The equation of motion over all four phases can be written in the form:

$$m(\ddot{y}_c + \ddot{y}_{m/c}) + ky_{m/c} + F_y = 0, \tag{1}$$

where F_y is a piecewise function that takes a value of zero in phases (i) and (iii), the no-contact phases. This force is a non-linear function of the distance traveled by the mass with respect to the chip in phase (ii), when the latch and mass are in contact. The static interaction between the mass and the latch is illustrated in Fig. 7. The associated forces are determined as

$$F_y = N \sin \theta + F_f \cos \theta, \tag{2}$$

$$F_x = N \cos \theta - F_f \sin \theta = k_1 x. \tag{3}$$

By examination of Fig. 7, geometrical relationships between x, y, and θ can be obtained as follows

$$\sin \theta = \left(\frac{y_0 - y_{m/c}}{2r} \right), \tag{4}$$

$$\cos \theta = \frac{\sqrt{4r^2 - (y_0 - y_{m/c})^2}}{2r}, \tag{5}$$

$$x = 2r \cos \theta - (r + d_i). \tag{6}$$

After substituting (6) into (3), one can solve for the normal force N, which in turn can be substituted into (2) to obtain F_y. This results in

$$N = \frac{k_1 x}{\cos \theta - \mu \sin \theta} = \frac{k_1 [2r \cos \theta - r - d_i]}{\cos \theta - \mu \sin \theta}, \tag{7}$$

$$F_y = \frac{k_1 [2r \cos \theta - r - d_i]}{\cos \theta - \mu \sin \theta}(\sin \theta + \mu \cos \theta). \tag{8}$$
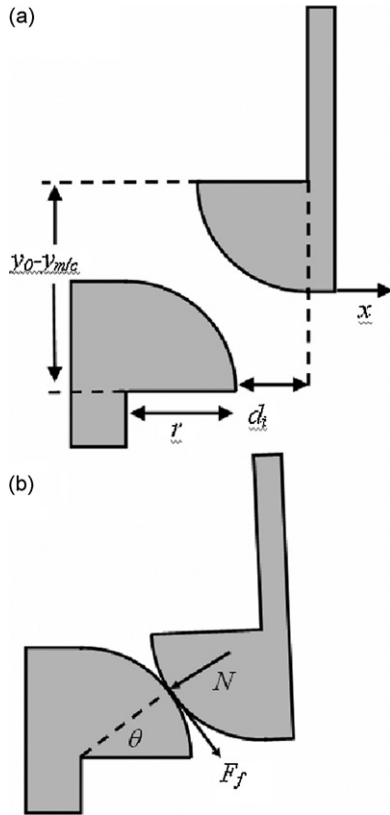
Fig. 7. Illustration of interaction between mass and latch: (a) geometrical relationships and (b) forces exerted by latch on mass.

Finally, F_y can be written as a function of y after substituting (4) and (5) into (8):

$$F_y = \frac{k_l \left(\sqrt{4r^2 - (y_0 - y_{m/c})^2} - r - d_i \right)}{\sqrt{4r^2 - (y_0 - y_{m/c})^2} - \mu(y_0 - y_{m/c})}$$

$$\times \left[y_0 - y_{m/c} + \mu \sqrt{4r^2 - (y_0 - y_{m/c})^2} \right] \quad (9)$$

The system (1) can be numerically solved by integrating the state-space form of these equations. To this end, the states

$y_1 = y_{m/c},$
$y_2 = \dot{y}_{m/c},$

are introduced and the state-space form is obtained as

$\dot{y}_1 = y_2,$
$\dot{y}_2 = -\ddot{y}_c - \dfrac{ky_1}{m} - \dfrac{F_y}{m}. \quad (10)$

Based on the states (y_1, y_2), the contact force F_y is turned on in phase (ii) and set to zero in phases (i) and (iii). For a quarter-circular latch and a quarter-circular mating piece on the mass, contact is first made when:

$$\cos \theta = \frac{r + d_i}{2r}. \quad (11)$$

and this contact is present till $y_{m/c} = y_0$.

The system parameters for the 37.5 g and 75 g acceleration designs are given in Table 1. These values were used to carry out the simulations. An estimate of the response time of the shock sensor is calculated as 1/4 of the free-vibration period, which for the present
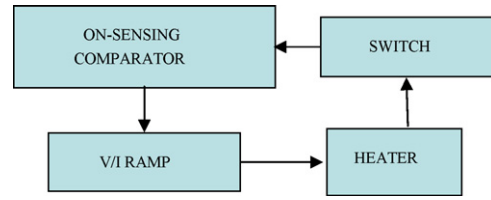

Fig. 8. A block diagram of the latch reset controller feedback loop. When the "switch" (the shock-sensing latch) is closed, current flows, heating the latch (the "heater" in the block diagram). The supplied heat eventually opens the latch, as sensed by the comparator. Once this opening is sensed, the power driver is turned off.

shock sensor results in a response time of 1.2 ms for the 37.5 g sensor design and 0.7 ms for the 75 g sensor design. The non-linear model predicts that the 37.5 g sensor will first latch at 21.9 g after 1.91 ms if the friction coefficient is zero and the minimum acceleration required to latch the sensor is applied as a step function at time zero. According to the model, the 75 g sensor will first latch at 49.2 g after 1.21 ms under the same conditions. The simulation results for non-zero values of the friction coefficient are discussed later in Section 5.

4. Circuit to sense latching, unlatch, and reset device

4.1. The basic controller

A low-power feedback control circuit has been designed to sense the latched state of the sensor and, after sensing, activate the reset actuators to unlatch and reset the device as described above. The goal of this control system is to achieve reset with minimum power expenditure. It is required that power not be drawn when the device is not latched, and a sleep mode has been included to ensure this. The circuit has also been designed to ramp up the power applied to the reset actuator during reset and immediately cut off power and go into a sleep mode when reset is achieved.

Since various designs are still being evaluated for the reset actuators, there are no set resistance or current/voltage requirements for the reset actuator operation. Therefore, the current driver is required to supply current for actuator resistances ranging from tens to hundreds of Ohms. This is done by creating a feedback network that ramps thermal energy into the system without overshoot.

The feedback network senses the latch opening and takes the drive current to zero when this occurs. A block diagram of this system is shown in Fig. 8. Here, the feedback loop and major system components are illustrated. In Fig. 9, the actual control circuit is provided. The MEMS latch is modeled as two resistances across P1 and P2. When the latch opens, P1 becomes infinite. The three power transistors represent the power driver of the network. These have the flexibility to source up to 8 amps of current to the latch through transistor Q6, although the reset actuators only use 70 mA per device. When the latch closes, voltage appears at the inverting input to U1A (the first loop operational amplifier). U1A, in turn, drives U1B that inverts the output signal allowing for a proper polarity input to the integrating operational amplifier U1C. U1C passes

Table 1
Shock-sensor parameters used for calculations

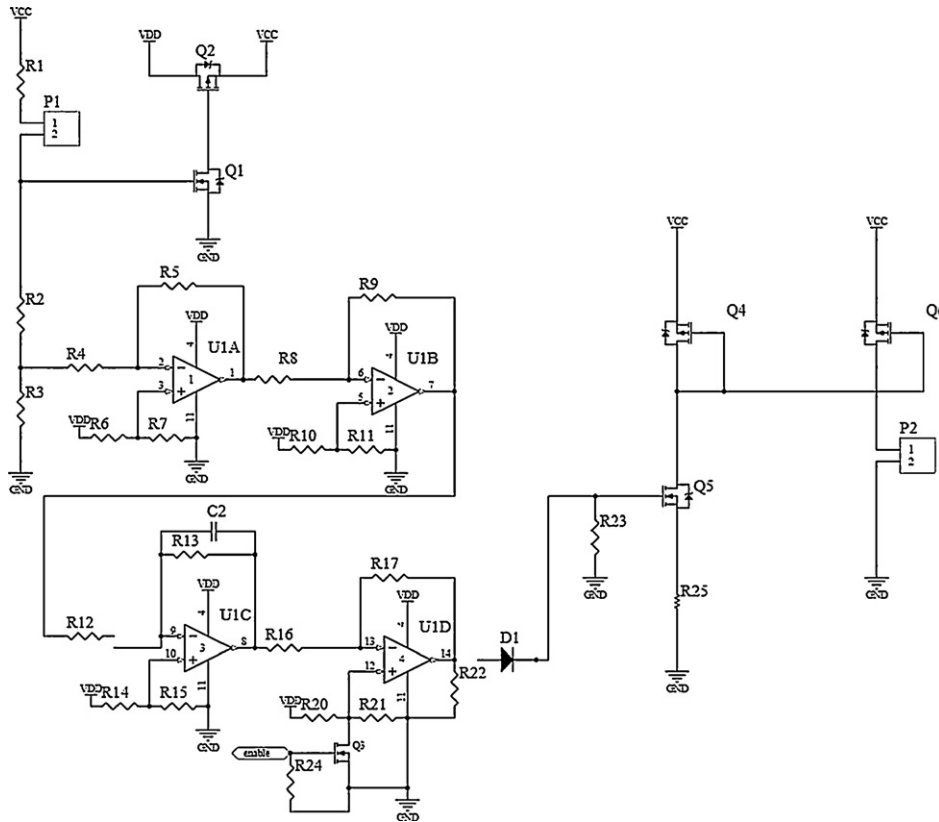| Sensor	37.5 g design	75 g design
m	3.42×10^{-7} kg	2.65×10^{-7} kg
k	0.601 N/m	1.32 N/m
k_L	3.4 N/m	3.4 N/m
y_0	150 μm	150 μm
Mass travel/g (prediction)	5.58 μm/g	1.97 μm/g
Reset current (experimental)	70 mA	70 mA
Reset deflection	28 μm	28 μm

Fig. 9. The MEMS latch reset current driver circuit.

a ramped output voltage to U1D, an amplifier whose gains are set by R16 and R17. The amplified ramp output drives Q5, lowering its channel resistance increasing the current through it. This current is mirrored in Q6, which sources current to the latch until it opens. When the latch opens, the input to Q5 goes to zero and no current flows through the drive transistors Q4 and Q6. Thus, the power dissipation is minimized, as determined by the on-state current of the operational amplifiers U1A–U1D.

This circuit was assembled by using commercial, off-the-shelf parts. The rise and fall characteristics of the controller have been characterized and these characteristics are shown in Fig. 10. The rise and fall times are set by the integrating capacitor, C2. The con-

figuration portrayed in Fig. 9 leads to a 1 ms rise and fall. The control system can be adjusted to minimize power overshoot by increasing or decreasing C2. The operating characteristics as designed are shown in Table 2.

It should also be pointed out that the voltage supplied to the non-inverting input of U1D is necessary for a voltage to appear at the output of this operational amplifier. Thus, this input serves as an "enable" for the circuit. It is possible in a malfunctioning device that a conducting bridge could form, which is not broken by the power supplied by the controller. In this case, it is necessary to power down the circuit to prevent supply drain. This can be accomplished by using the output voltage from Q2 to trigger a countdown circuit that supplies the necessary voltage at the onset of the count and zeros after some pre-determined period, shutting the power driver off, even if there is still a conducting bridge present. This time-out circuit is described in greater detail in the next section.

4.2. Description of the fail-safe time-out circuit

The time-out circuit protects against unnecessary power drain due to a malfunctioning device that cannot be reset. A circuit diagram for the time-out circuit is shown in Fig. 11. After the circuit counts a pre-determined number of milliseconds of "on-state" operation of the current source, the "enable" signal is withdrawn from the non-inverting input of the operational amplifier U1A
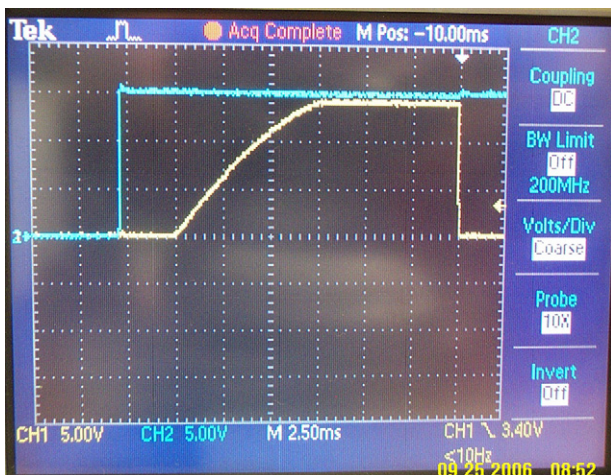

Fig. 10. Turn on and turn off characteristic of the power driver for the controller.

Table 2
Characteristics of the control circuit

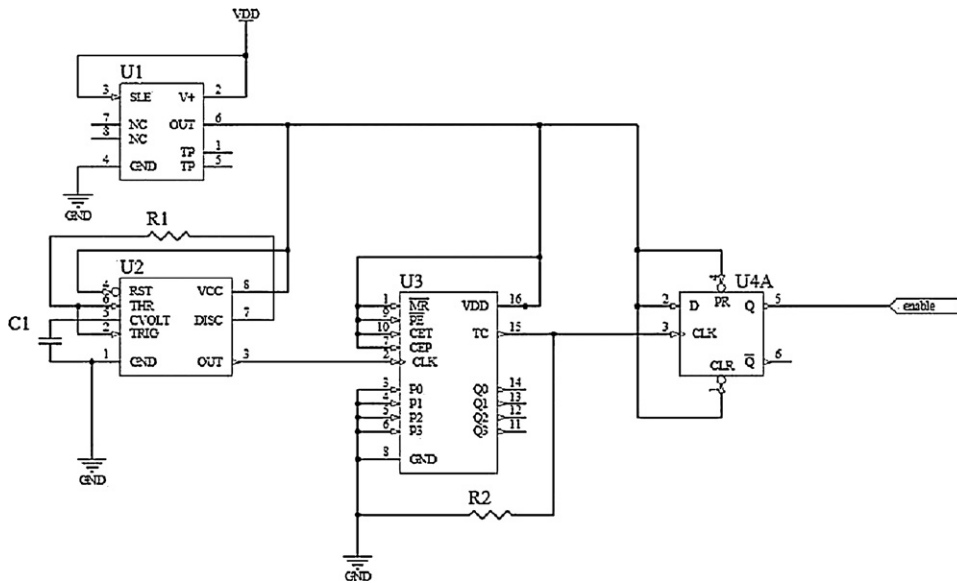| Element	Value
QUIESCENT POWER	<1 nW
RISE TIME	1–10 ms
FALL TIME	<1 ms

Fig. 11. Fail-safe shut-off timing circuit.

(node 3 of U1A in Fig. 9). This open switches all supplies, sending the control loop into a sleep mode. No power is drawn from the supplies at this point. The three sub-circuit elements are discussed next.

TIMER—the timer chip generates the square wave output signal for the COUNTER. It contains an RC circuit in which the selection of R and C values set the frequency; here, this is chosen to generate a 1-kHz clock signal. For the purposes of this demonstration, a TLC555IP chip was used.

COUNTER—the counter chip takes the Clock signal as input and generates a trigger output signal, D Clock, for the D FLIP FLOP. The trigger signal is taken to be the carry output signal of the counter. For the purposes of this demonstration, a 74ACT161PC chip was used.

D FLIP FLOP—the d flip flop (positive edge triggered) chip takes the D Clock signal as input and generates the overall timing circuit Output. The Output signal remains low as long as the D Clock signal does not switch. When the D Clock signal switches from low to high, the Output signal then switches high and remains high. For this demonstration, a 74ACT74PC chip was used. *Note*: a voltage regulator, not shown, supplies voltage to this circuit. The regulator is connected to the MEMS Heat Controller main supply lines. Hence, when power is shut-off to the entire board, so too is the power to the timing circuit.

5. Results and discussion

Shock sensors were fabricated according to the design and process flow detailed above. Some were made without cap chips to facilitate visual inspection of the sensor to determine the latched state while testing. Shock sensors were designed to latch at various levels of shock, without knowing the friction coefficient beforehand. To test the shock level at which a sensor latches, a GHI linear shock machine was used with the sensors glued to a fixture bolted to the shock table. The shock table uses a spring that is compressed to a defined setback position and then released to allow the table to accelerate and hit a physical stop. The shock pulses obtainable from the shock machine range from 0.1 ms to 30 ms duration, with peak acceleration values between about 10 g and 2000 g, depending on the initial spring compression and the hardness of the physical stop.

The sensors that were studied in this effort operate mainly in the range of 25–100 g with response times of a few milliseconds. The shocks applied in testing were half-sine in shape, with durations of about 8.4 ms. Latching was confirmed visually by using a magnifier. Data on several sensors designed to latch at one of two different levels were collected. The average shock magnitude required to achieve latching is plotted in Fig. 12, along with the experimental data and data spread over the different experiments. Seven devices of each device type were studied. Repeated friction testing on test devices fabricated in the same process flow was presented in Ref. [9]. No change in the friction coefficient was observed with multiple (10+) cycles for DRIE sidewalls with similar surface roughness to the devices tested here. More extensive testing of larger sample sets and repeated testing of individual devices is to be undertaken in future work.

The model presented in Section 3 was applied to both designs by using a best fit to the average shock values to determine the equivalent sliding friction coefficient. To obtain the best fit friction coefficient, the model was run with varying friction coefficients keeping all other parameters as designed, and the model predicted values of acceleration required to latch the devices were compared with the test data. In making this comparison, outliers in the test
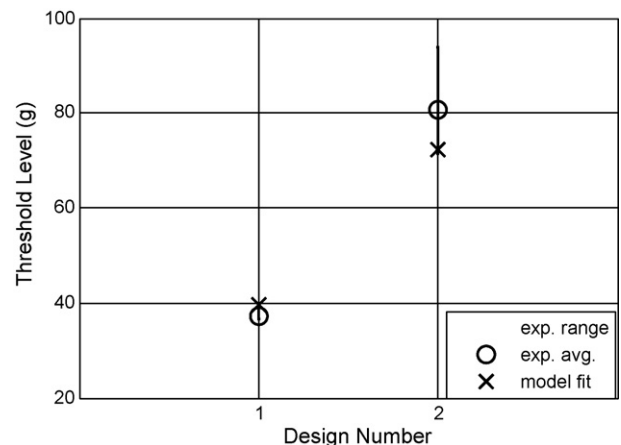

Fig. 12. Shock table test data for two threshold levels plotted with model best fit.

data were excluded, as these invariably required far higher shock pulses to latch. This is believed to be due to stiction in the device, which is not accounted for in the model. The model prediction obtained by using the best fit friction coefficient is also plotted in Fig. 12. The friction coefficient that produced the best fit is 0.47. This is lower than the measured static friction value of 0.7 [9], as it should be for a sliding interaction. The dynamic friction measurement has not been performed as yet to verify the friction value used to obtain the model fit. The model prediction matches the average of the experimental measurements to within 7.1% for Design 1 (37.5 g case) and 10.2% for Design 2 (75 g case). By using the best fit found for the sliding friction coefficient (0.47), the model predicts latching at 39.7 g after 1.2 ms for the 37.5 g sensor and 72.4 g after 0.91 ms for the 75 g sensor. Referring to the model of Section 3, the acceleration required for the sensor to latch is predicted to increase by 47% for the 75 g sensor and 81% for the 37.5 g sensor when friction is introduced. The latch times appear to decrease from those predicted in Section 3 because the applied acceleration is increased; however, given the same acceleration, the model predicts a lower time to latch for the frictionless case.

Packaged sensors have also been produced, but these have not been tested on the shock table because electrical confirmation of latching is unreliable at this point. The contact resistance is too high and too variable over repeated latching events (variation between 2 MΩ and 50 MΩ). This is due to poor contact resistance and poor adhesion of the contact metal to the latch sidewalls. Improvements need to be made on the contact metal process to lower the contact resistance and achieve better repeatability. A cleaning step using piranha or oxygen plasma to remove polymer residue left on the sidewalls using DRIE should solve this problem.

During the experiments, some sensors were observed to be stuck down to the substrate and they could not be disturbed to move or latch due to the in-plane shock. They can be unstuck manually by pushing with a probe, but they readily stick to the handle wafer again. This does become a problem with more elapsed time after a release. Devices were stored indoors at ambient conditions. It is not yet known whether the stiction is related to humidity or electrostatic effects. If the issue is humidity, vacuum packaging should help here, but this has not been confirmed. Failures which have stiction attributes have been observed in the packaged sensors, but inspection is difficult and the cause of these failures is unconfirmed as of this writing. With a thicker device layer, the sensors would also not be as prone to stiction because of a higher out-of-plane stiffness. The design is insensitive to thickness because both the mass and in-plane stiffness of the springs scale linearly with device layer thickness. The drawbacks to this solution are that the minimum gap (3 μm between the release actuator and latch) may be difficult to resolve through standard DRIE processes as the device layer thickness is increased past 30 μm or so, and also, the reset actuator power will increase linearly with thickness as well.

6. Conclusions

A latching shock sensor has been presented, which has potential for acceleration monitoring over long time spans (several years) with limited available power. Further work towards improving device reliability (primarily elimination of stiction failures) is needed to realize this potential. A preliminary model to aid in the design and prediction of device performance has been presented, including prediction of the device response time. A detection, sensing, and activation circuit for the shock sensor reset has been developed and described. Experimental studies with the shock sensor have been performed and the results have been compared to the model predictions by applying a best fit to the unknown friction coefficient. Friction studies are underway to confirm this friction coefficient by using the friction test structures presented in recent work [9]. The experimental studies have allowed the authors to characterize the following system shortcomings: (i) the latched contact resistance is too high and (ii) stiction is a problem. Improvements are to be made to the sidewall metallization to lower the contact resistance and coatings and structural changes are to be investigated to alleviate stiction.

References

[1] H. Van der Auweraer, International research projects on structural health monitoring, Structural Health Monitoring 2 (2003) 341–358.
[2] J.P. Lynch, K.J. Loh, A Summary review of wireless sensors and sensor networks for structural health monitoring, Shock and Vibration Digest 38 (2006) 91–128.
[3] D. Ciarlo, A latching accelerometer fabricated by the anisotropic etching of (1 1 0) oriented silicon wafers, Journal of Micromechanics and Microengineering 2 (1992) 10–13.
[4] X-Q. Sun, S. Zhou, W.N. Carr, A surface micromachined latching accelerometer, Transducers (1997) 1189–1192.
[5] M.R. Whitley, M. Kranz, R. Kesmodel, S. Burgett, Latching shock sensors for health monitoring and quality control, Proceedings of SPIE 5717 (2005) 185–194.
[6] C.D. Lott, T.W. McLain, J.N. Harb, L.L. Howell, Modeling the thermal behavior of a surface-micromachined linear-displacement thermomechanical microactuator, Sensors and Actuators A 101 (2002) 239–250.
[7] L. Que, J.-S. Park, Y.B. Gianchandri, Bent-beam electrothermal actuators-part 1: single beam and cascaded devices, Journal of Microelectromechanical Systems 10 (1999) 247–254.
[8] J.M. Maloney, D.S. Schreiber, D.L. DeVoe, Large-force electrothermal linear micromotors, Journal of Micromechanics and Microengineering 14 (2004) 226–234.
[9] L.J. Currano, M. Yu, B. Balachandran, Novel Friction test structures for microelectromechanical systems, in: Proceedings of the ASME International Mechanical Engineering Congress and Exposition, 2006, p. 14054.